PCCP

ROYAL SOCIETY OF CHEMISTRY

PAPER

View Article Online
View Journal | View Issue

Cite this: *Phys. Chem. Chem. Phys.*, 2025, **27**, 20838

Quantum tunneling dynamics in the Ni^+-mediated C–H activation of acetic acid

Gabriele Pinto, Hamed Barzinmehr, Simon U. Okafor, William Smith, Michael Brdecka, Katie L. Benjamin, Michael Gutierrez and Darrin J. Bellert *

The mechanistic and dynamic properties of the Ni^+ mediated reaction with CH_3COOH and its perdeuterated isotopologue are presented. Microcanonical kinetic measurements are made in the gas phase with the energy- and time-resolved single photon initiated dissociative rearrangement reaction (SPIDRR) technique and these are complemented with density functional theory (DFT) and multi-reference (MRCI) calculations. Experimental and theoretical evidence indicates that the formation of three product pairs – $Ni(C_2H_2O)^+ + H_2O$, $Ni(CH_4O)^+ + CO$ and $Ni(H_2O)^+ + C_2H_2O$ – are rate limited by C–H bond activation. Measurements of rate-limiting microcanonical $k(E)$ rate constants are made over the 15 000 cm^{-1} to 20 000 cm^{-1} (180–240 kJ mol^{-1}) energy range where a transition from quantum mechanical tunneling to over-barrier reaction control is observed. Rate constants, where quantum mechanical tunneling (QMT) primarily contributed to their magnitudes, possessed a large H/D QMT kinetic isotope effect (KIE = 19.0 ± 3.2) consistent with the expectations of QMT. Surprisingly, QMT rate constants in the tunneling energy regime were nearly energy independent and appear to extrapolate to very low energies. Applications of tunneling corrections to RRKM (Rice–Ramsperger–Kassel–Marcus) calculated rate constants failed to describe this unexpected QMT behavior. It is proposed that the Ni^+ cation's electronic structure may promote QMT by providing bonding schemes where the proximity of organic fragments increase QMT probability. Such structures are proposed to exist along the multi-dimensional PES, providing tunneling pathways with reduced barrier widths and consequent energy dependence. These results highlight quantum dynamic properties of Ni^+ ions in C–H bond activation reactions, an important step towards understanding the metal's ability to promote catalysis at low energy.

Received 9th July 2025,
Accepted 31st August 2025

DOI: 10.1039/d5cp02626a

rsc.li/pccp

1 Introduction

Heterogeneous catalysis is an essential feature in modern industrial chemistry, enabling efficient and selective reactions with a wide range of applicability. These catalysts operate at solid–gas or solid–liquid interfaces, offering advantages such as recyclability, stability, and ease of separation. Heterogeneous catalytic activity is largely dictated by the surface defects of the solid phase. At these sites, the unsaturation and accessibility of surface metal atoms make them electronically distinct from the bulk, priming them for catalytic activity by their bonding interactions with a substrate.

Unsaturation, accessibility, and quantized electronic structure are properties that are further exploited by recent advances in single-atom catalysts[1–9] and nanoparticles.[2,10–18] Scaling down the catalytic active site from surface defects to nanoparticles or even a single atom has further enhanced heterogeneous catalytic efficiency by optimizing metal utilization and providing well-defined active sites. As technology continually miniaturizes the solid phase, it becomes evident that quantum mechanical properties will play increasingly crucial roles in the improvements of modern catalysts.

Understanding the contributions of quantum dynamic processes to catalysis and bond activation is, however, a challenging task, as those non-classical phenomena take place in classical environments during the catalytic process. Fortunately, the unsaturation and accessibility of metal ions in heterogeneous catalysis are qualities shared with support-free metal ions participating in gas-phase reactions. Gas phase studies may therefore serve as valuable tools for understanding catalytic mechanisms and dynamics free from solvation and transport interferences. Thereby the effects of quantum phenomena on the catalytic function and dynamic properties of the metal may be appropriately elucidated.

Among transition metals, nickel (Ni) is widely employed in homo- and heterogeneous catalysis due to its exceptional catalytic versatility in carbon bond activation reactions, including olefin polymerization,[19–23] metathesis cycloaddition,[24–31] methanation,[32–38] carboxylation,[39–45] and transamidation.[46–52]

Baylor University, 1311 S 5th St, Waco, TX 76706, USA.
E-mail: Darrin_Bellert@baylor.edu

For instance, Ni nanoparticles supported on TiO_2 are extensively used in cross-coupling reactions,[17,18,53] U_3O_8-supported Ni catalysts efficiently convert CO_2 in methanation,[54] and zeolite-supported Ni catalysts demonstrate superior selectivity in ethanol to hydrocarbon conversion.[55] The catalytic versatility of Ni in carbon bond activation reactions makes it a subject of interest to study the effects of quantum dynamics on reaction rates and catalytic efficiency.

In this work, the reaction between bare Ni^+ ions and CH_3COOH is investigated using the single photon initiated dissociative rearrangement reaction (SPIDRR) technique,[56] enabling the measurement of microcanonical rate constants in an environment free of collisions and other reaction-perturbing effects. In the nominal reaction, Ni^+ participates in selective C–C and C–H bond activations through an oxidative addition/reductive elimination (OA/RE) sequence. CH_3COOH serves as the ideal organic substrate because of the presence of both methyl and carboxylic hydrogens, providing a single source of C–H bond activation and two distinct candidates for selective D-labeling.

QMT has been shown to significantly influence C–H bond activation rates in both heterogeneous and enzymatic catalysis.[57,58] However, the specific roles that transition metals play toward influencing QMT remains largely unexplored. This is likely due to experimental challenges associated with isolating such contributions as this demands specialized instrumentation. The SPIDRR technique was developed with the requisite high energy and temporal resolution required to confidently interpret such metal facilitated QMT phenomena. In fact, SPIDRR has been previously employed to measure rates of QMT in the microcanonical, Co^+ mediated decomposition of acetic acid and acetaldehyde.[59,60]

In this study, the microcanonical kinetics of $Ni(CH_3COOH)^+$ decomposition and its perdeuterated isotopologue CD_3COOD are measured, and significant tunneling is identified through measurement of a high kinetic isotope effect (KIE). We henceforth provide experimental evidence of the mechanistic steps in the reaction, of rate-influencing potential energy surface (PES) features, and of efficient QMT with surprising rates of $>10^5$ s^{-1} which appear nearly energy independent.

By integrating experimental and computational approaches, this study deepens our understanding of nickel's role in C–H bond activation, especially in facilitating QMT. Comparison between gas-phase experiment and computational results at different levels of theory will further provide an ideal arena to refine computational models. These insights may help explain the catalytic and enzymatic activity of Ni^+ and inform the design of next-generation heterogeneous and biomimetic catalysts with improved activity, selectivity, and efficiency for various chemical applications.

2. Procedure

2.1 Experimental procedure

A detailed explanation of the technique and instrument has been previously published.[56] SPIDRR kinetic measurements are performed under high-vacuum ($\sim 10^{-3}$ Pa) within a 120 L expansion chamber that is orthogonally coupled to a 186 cm time-of-flight mass spectrometer (TOF). The Ni^+ ions are generated in the expansion chamber by ablating a rotating nickel rod using focused 15 mJ pulsed 532 nm output from a frequency-doubled Nd-doped yttrium aluminum garnet (Nd:YAG) laser.

The Ni^+ ions are entrained in a pulsed helium supersonic expansion seeded with the vapor pressure of CH_3COOH or its perdeuterated isotopologue. The metal ions and organic molecules collide and react to form the various cationic complexes shown in the lower panel of Fig. 1. These ions are subsequently cooled in the adiabatic jet expansion. The translational temperature of the $Ni(CH_3COOH)^+$ cluster is 50 mK as determined from fits of its measured velocity distribution within the beam (Fig. SI-1).

Effective vibrational cooling is indirectly assessed by doping the expansion with small amounts (1–2%) of CH_4 gas.[61–64] Doping small quantities of polyatomic molecules into the expansion increases the efficiency of vibrational cooling through collisional energy transfer to the CH_4's vibrational modes. Agreement between measured rate constants under CH_4-doped and neat (undoped) expansion conditions suggests efficient vibrational cooling under both expansion conditions (see Fig. SI-2 for a comparison at 17 500 cm^{-1} laser energy for $Ni(CH_3COOH)^+ \rightarrow Ni(H_2O)^+ + C_2H_2O$ rearrangement reaction). The large spin–orbit coupling in the Ni^+ ion[65] ensures that no electronic metastable precursors exist in the molecular beam, thus ensuring electronic cooling. Electronic and vibrational

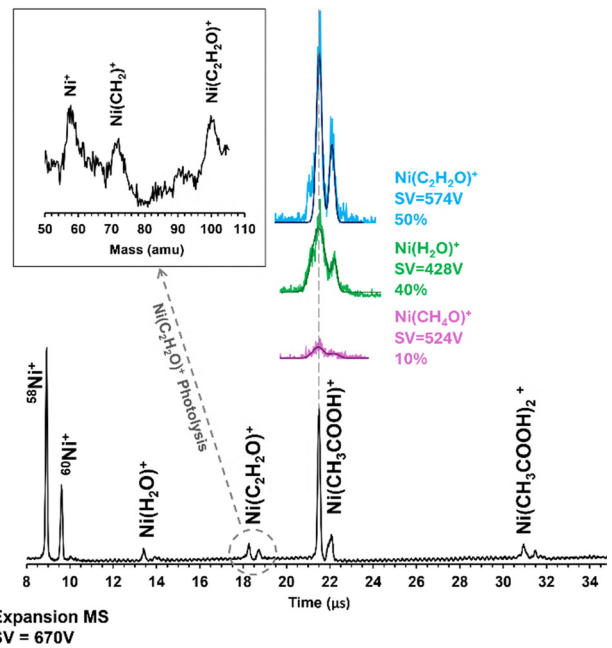

Fig. 1 TOF-MS of the ions in the supersonic expansion (lower black trace), with overlaid MS of the rearrangement reaction products of the $Ni(CH_3COOH)^+$ encounter complex: $Ni(CH_4O)^+$ (purple), $Ni(H_2O)^+$ (green) and $Ni(C_2H_2O)^+$ (blue). Transmission voltages (SV) through the hemispherical sector and exit channel fractions (ECF) are provided. Inset: Fragmentation pattern of $Ni(C_2H_2O)^+$ mass peak resulting from photolysis of the ion by a focused 355 nm photon beam.

cooling preserves the microcanonical environment of SPIDRR measurements, allowing us to approximate the internal energy of the precursor at the absorbed photon's quantum.

The jet-cooled species are extracted from the He expansion into the TOF by voltage pulse to an orthogonal accelerator (OAc). The cations, including the electrostatically bound precursor or reactant complex (**RC**), $Ni(CH_3COOH)^+$, are accelerated to the same kinetic energy and separated by mass according to their flight time. Dissociation products generated within the field-free region of the TOF are separated by transmission through a voltage-tuned hemispherical analyzer following their free flight. Hence, product arrival time at the Chevron microchannel plate (MCP) detector is determined by the **RC** mass, while the transmission voltage (SV) selects the product dissociated within the TOF. The laser-initiated dissociative rearrangement kinetics are studied by energizing the **RC** in the expansion with the output of an Nd:YAG-pumped tunable dye laser.

The ground and electronic excited states of the electrostatically bound **RC** are best described as combinations of the ground and low-lying atomic states of Ni^+ with the ground electronic state of CH_3COOH ($^1A'$). In such fashion, we identify the **RC** ground state[66] as $Ni^+(^2D, 3d^9)\cdot CH_3COOH$. The Ni^+ is the chromophore which absorbs a photon's quantum in the 15 000–20 000 cm^{-1} (180–240 kJ mol^{-1}) energy range, exciting the doublet ground state of the **RC** to an excited doublet. The likely electronic transition is $Ni^+(^2F, 3d^84s)\cdot CH_3COOH \leftarrow Ni^+(^2D, 3d^9)\cdot CH_3COOH$. The transition is spin-allowed but parity forbidden, with a TD-DFT computed oscillator strength of 5.985×10^{-6}. Few of the **RC** molecules will absorb the photon, and because of the low transition probability, the excited ^2F population will not appreciably decay by emission before entropically-driven internal conversion (IC) takes place.

The ground state binding energy of the electrostatic $^2Ni(CH_3COOH)^+$ complex is 21 821 cm^{-1} (261 kJ mol^{-1}), calculated with basis set superposition error corrected DFT (B3LYP/def2-tzpv). Given that the spin–orbit averaged $Ni^+(^2F, 3d^84s) \leftarrow Ni^+(^2D, 3d^9)$ atomic promotion energy is ~13 550 cm^{-1} (162 kJ mol^{-1}), the vibrational states of the excited electronic $Ni^+(^2F, 3d^84s)\cdot CH_3COOH$ state exists in effective degeneracy and overlap with the high vibrational levels of the ground $Ni^+(^2D, 3d^9)\cdot CH_3COOH$ state. Over the energy range of our measurements, the ground: excited vibrational density of states ratio is 10^5–10^8 (see Fig. SI-3). Hence, entropically driven IC should immediately follow photon absorption as the vibronic **RC** energy is redistributed from the relatively sparse vibrational states of the excited doublet into the much denser excited vibrational states of the ground **RC** entrance well. Moreover, the electronic coupling between these states may be gauged by photodissociation action studies of simpler $Ni(L)^+$ species (L = Ar, CO_2, H_2O) where vibronic resonances have been resolved.[67–69] The action that permits detection in these studies is the vibronic coupling between the excited bound state and a repulsive state that ultimately couples into the dissociative continuum of a lower PES. The upper state lifetime is very short with dissociation occurring within a microsecond following photon absorption. This suggests strong electronic couplings between states that would extend to larger, more complex systems.

Following IC internal vibrational redistribution (IVR) occurs on the nanosecond scale to distribute the supplied photon energy across the dense vibrational states (10^{10}–10^{12} states cm^{-1}). Each of these states is described by a combination of 21 vibrational quantum numbers, which changes with system energy. Thus, there exists an everchanging distribution of vibrational quantum states in the ground electronic state as the energy content to the system is modified.

The **RC** is thus prepared with a resolved high-vibrational-energy content to proceed along reactive pathways on the ground state PES. This process can be summarized as:

$$Ni^+(^2D, 3d^9)\cdot CH_3COOH,\ \text{ground vibrational} \xrightarrow{h\nu}$$

$$Ni^+(^2F, 3d^84s)\cdot CH_3COOH,\ \text{excited vibrational} \xrightarrow[\text{(b)IVR}]{\text{(a)IC}}$$

$$Ni^+(^2D,\ 3d^9)\cdot CH_3COOH,\ \text{high vibrational} \xrightarrow{\text{OA/RE}} \text{Rearr. Products}$$

The short time scale of the electronic processes provides a resolved start time for the reaction, which is rate-limited by the kinetics of nuclear motion within the OA/RE sequence. Moreover, due to the collision-free trajectories of the **RC** ions in our system's high vacuum and the efficient jet cooling, the internal energy of each ionic complex is determined by the absorbed photon's energy. This ensures that microcanonical rate constants are measured at highly resolved energies. We emphasize that temperature is not defined in the photoexcited microcanonical system as the energy content is not determined by a Boltzmann distribution. Instead, energy is the controlled variable and these unique defining characteristics of the SPIDRR technique provides the requisite high time and energy resolution to confidently interpret dynamics.

Single photon absorption initiates chemical reactions in the SPIDRR technique and is validated through the measured linear dependence of a rearrangement product's intensity on laser fluence (Fig. SI-4). Multi-photon absorption processes excite the **RC** to energies above the cluster dissociation limit. Such occurrences do not interfere with our kinetic measurements as the **RC** dissociates into its electrostatic components as opposed to its OA/RE rearrangement products.

Reaction initiation time is controlled by timing when the laser pulse intersects the cold molecular beam. The dissociative rearrangement reaction is thereby initiated prior to acceleration into the TOF chamber. This effectively reduces the number of **RC** molecules that will form products within the TOF. SPIDRR signal, S_{SPIDRR}, is measured as the product voltage detected at the MCP and is therefore proportional to the number of product cations formed within the field-free region of the TOF. This depends on the delay τ between the reaction

initiation and orthogonal acceleration according to eqn (1):

$$S_{\mathrm{SPIDRR}} \propto P_{(t=|\tau|+\alpha+\Delta)} - P_{(t=|\tau|+\alpha)} = \int_{|\tau|+\alpha}^{|\tau|+\alpha+\Delta} \frac{\mathrm{d}P}{\mathrm{d}t}\mathrm{d}t \propto \mathrm{e}^{-k|\tau|} \quad (1)$$

Here, Δ represents the time spent in the field-free TOF and α denotes the time spent by the **RC** in the OAc. In general, the maximum SPIDRR signal is produced at τ = 0. $\mathrm{d}P/\mathrm{d}t$ is proportional to **RC** decay and as $|\tau|$ increases, more **RC** molecules decay into products prior to orthogonal abstraction. These products are not detected within the **RC** time-gate and do not contribute to product yields. The result is that the SPIDRR signal decreases exponentially, with the limiting rate constant determined by fitting $S_{\mathrm{SPIDRR}}(\tau)$ to exponential functions (eqn (1)).

Measurements of the Ni^+ mediated dissociative rearrangement of CH_3COOH were repeated at various activating photon energies, selected by tuning the output frequency of the dye laser. Laser fluence, and consequently SPIDRR signal intensity, depends on the dyes' wavelength-dependent conversion efficiency. This hinders measurements for some of the less intense reaction products at specific energies. Furthermore, SPIDRR measurements were repeated with the isotopically labeled species CD_3COOD. Microcanonical rate constants $k(E)$ for both isotopes were obtained and the KIE (k_H/k_D) determined. These measurements allowed us to measure reaction rates $k(E)$, elucidate the reaction mechanism, and quantify the contribution of QMT in the titular reaction.

2.2 Computational methods

Structures for the **RC**, products and suggested intermediates and transition states were optimized using density functional theory (DFT) at the B3LYP level with the def2-TZVP basis set in Gaussian 16.[70] Frequency calculations at the same level confirmed the nature of stationary points (minima or transition states). Rice–Ramsperger–Kassel–Marcus (RRKM) calculations with Wentzel–Kramers–Brillouin (WKB),[71,72] small curvature (SCT)[73–75] and large curvature (LCT)[75–80] tunneling corrections were also performed. These used the vibrational frequencies computed at the DFT level. Additionally, multireference CASSCF/CASPT2 (complete active space self-consistent field)[81] single-point corrections were performed with the def2-TZVP basis set in ORCA,[82,83] with active spaces determined from RI-MP2 (Resolution of Identity Second-Order Møller–Plesset Perturbation Theory)[84] natural orbital occupation analysis. This resulted in an active space of 8 orbitals occupied by 9 electrons.

To ensure that the DFT geometries are appropriate for multireference single-point refinements, we compared the B3LYP/def2-TZVP and CASSCF(9,8)/def2-TZVP optimized $\mathbf{TS_3}$ structures, obtaining a root-mean-square deviation of 0.115 Å. This close agreement demonstrates that the two optimization levels describe essentially the same transition-state geometry, and that the CASPT2 refinement is being performed on a physically meaningful structure.

3 Results

3.1 Experimental determination of reaction mechanism

3.1.1 Supersonic expansion MS. Fig. 1 presents the experimental investigations of the reaction mechanism by three distinct mass spectrometric techniques. First, the bottom trace in Fig. 1 presents the TOF mass spectrum showing the distribution of ions generated by the interaction of the Ni^+ ions in the laser vaporization source with CH_3COOH molecules and entrained in supersonic expansion. These ionic species are extracted from the molecular beam and accelerated by the OAc, which imparts a set amount of translational kinetic energy to the ions. The voltage difference applied to the halves of the hemispherical sector allows transmission of the ionic species traveling with this full kinetic energy. The major ions identified in the expansion are the bare $^{58}Ni^+$ and $^{60}Ni^+$ atomic ions, the reactant complex $Ni(CH_3COOH)^+$, the reaction products $Ni(H_2O)^+$ and $Ni(C_2H_2O)^+$, and lastly the dimer $Ni(CH_3COOH)_2^+$. We note that the intensity of the $^{60}Ni(CH_3COOH)^+$ cluster is artificially reduced from its natural abundance due to the MCP recovery time.

3.1.2 Products MS. The **RC** in these kinetic studies is the 58 and 60 isotopes of the $Ni(CH_3COOH)^+$ monomer. Time-gating over its arrival time at the MCP and scanning the voltage difference across the hemispherical sector allows the determination of the **RC**'s dissociation product masses. These arrive at the MCP at the same time as the **RC** but are transmitted at different SV. The mass spectra of the $Ni^+(CH_3COOH)$ photoinitiated reaction products, measured at a laser energy of 16 600 cm^{-1} and at their optimal transmission SV, are shown in Fig. 1 as the colored traces. The acquisition of product mass spectra represents the second method used to suggest a reaction mechanism. The reaction products are the 58 and 60 isotopes of $Ni(H_2O)^+$, $Ni(CH_4O)^+$, and $Ni(C_2H_2O)^+$ and are represented respectively in purple, green and blue. Product ion intensities are determined by summing the integrated Gaussian fits for each 58 and 60 isotopes of each product measured at τ = 0. Product exit channel fraction (ECF) is determined through ratios of the integrated product intensities. The ECF for these products (40 : 10 : 50 ordered by mass) is the same at all measured photon energies. The measurements presented as the colored traces in Fig. 1 indicate the following reaction channels with rearrangement products assigned:

$$\mathrm{Ni(CH_3COOH)^+} \xrightarrow{h\nu} \begin{array}{l} \mathrm{Ni(H_2O)^+ + C_2H_2O\ (ECF = 40\%)} \\ \mathrm{Ni(CH_4O)^+ + CO\ (ECF = 10\%)} \\ \mathrm{Ni(C_2H_2O)^+ + H_2O\ (ECF = 50\%)} \end{array} \quad (R1)$$

Analogous products are measured for the 58 and 60 isotopes of the Ni^+ mediated rearrangement of the CD_3COOD isotopologue. The corresponding change in transmission voltage for the isotopically labeled products is consistent with the assigned product identities. Dissociation of $Ni(CD_3COOD)^+$ proceeds with (30 : 10 : 60) ECF, indicated as low to high product mass, and again consistent through all measured energies (Fig. SI-5).

3.1.3 Photolysis. We employ photolysis of specific mass spectral features as a third technique that informs the reaction mechanism by suggesting product structure.[85,86] The lowest trace of Fig. 1 shows two mass peaks between the Ni^+ atom and the $Ni(CH_3COOH)^+$ species. These mass peaks are assigned as $Ni(H_2O)^+$ and $Ni(C_2H_2O)^+$. Interestingly, these species are the two most intense products from the photon initiated, Ni^+ mediated decay of CH_3COOH (blue and green traces in Fig. 1 and reaction (R1)). This leads us to believe that the $Ni(H_2O)^+$ and $Ni(C_2H_2O)^+$ mass peaks evident in the mass spectrum result from the unquenched reaction of $Ni^+ + CH_3COOH$ that occurs in the laser driven source prior to supersonic cooling. Thus, experiments designed to suggest these species' structures in turn suggest the structures of these two products in reaction (R1). Intense, focused 355 nm laser radiation is timed to photolyze each of these mass peaks just prior to entering the hemispherical sector. The resulting fragmentation pattern is determined by scanning the SV to transmit and detect charge fragments. Predictably, laser photolysis of the mass peak assigned to $Ni(H_2O)^+$ yielded the Ni^+ fragment only. More interesting, however, is laser photolysis of the mass peak assigned to $Ni(C_2H_2O)^+$ where the fragmentation pattern is seen as the inset of Fig. 1. Here, two fragment peaks are assigned as Ni^+ and $Ni(CH_2)^+$, suggesting that both CO and C_2H_2O are viable leaving groups. This further suggests that the $Ni(C_2H_2O)^+$ mass peak (Fig. 1) contains two structural isomers: the $Ni(C_2H_2O)^+$ electrostatically bound complex and the $Ni(CH_2)(CO)^+$ carbenoid species. These two isomers likely play important roles in the mechanism for the Ni^+ mediated decomposition of CH_3COOH. This is supported by the DFT calculated PES for this system which is presented below.

3.1.4 SPIDRR kinetic signature. Fig. 2 presents the kinetic signature of the formation of three products $Ni(CH_4O)^+$, $Ni(H_2O)^+$ and $Ni(C_2H_2O)^+$, and of their perdeuterated analogues, measured at an activating laser energy of 16 600 cm^{-1}. The *x*-axis is the variable τ, or the delay between laser initiation of the reaction and entrance of the **RC** into the OAc. By systematically increasing $|\tau|$, reduced reaction times are sampled, resulting in the observed exponential profiles, from which the rate constants for the dissociative rearrangement of $Ni(CH_3COOH)^+$ and of $Ni(CD_3COOD)^+$ are measured. In Fig. 2, the product intensities are normalized to highlight the agreement between each measured and fitted (solid curve) exponential profile.

3.1.5 Kinetic model. The formation kinetics of $Ni(CH_4O)^+$, $Ni(H_2O)^+$ and $Ni(C_2H_2O)^+$, crosses, Fig. 2, when independently fit to a single exponential function, yield rate-determining reaction rate constants which agree within the error of each independent fit. The same is true for the formation kinetics of the deuterated analogs $Ni(CD_4O)^+$, $Ni(D_2O)^+$ and $Ni(C_2D_2O)^+$, circles, Fig. 2. These similarities in each isomer extend to all laser energies used in this study. This indicates that the decay of a single reaction intermediate rate limits the formation of each of these products and that the reaction must trifurcate following this intermediate's decay. The simplest kinetic model to provide such features is presented in Scheme 1. In this

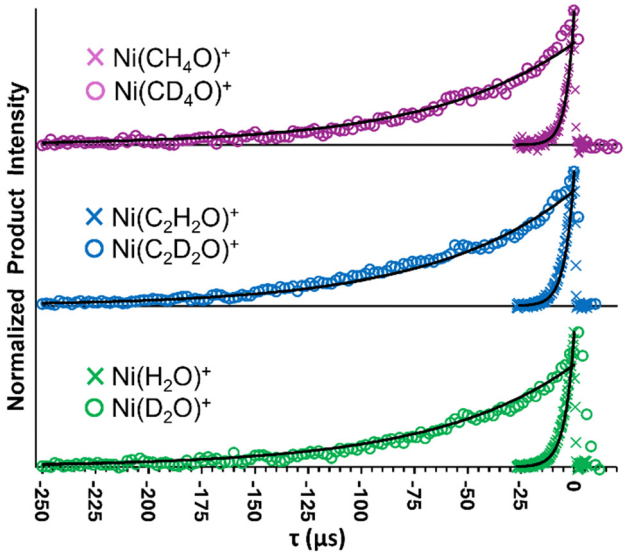

Fig. 2 SPIDRR kinetics measured at an absorbed 16 600 cm^{-1} (198.6 kJ mol^{-1}) photon energy in the decomposition of $Ni(CH_3COOH)^+$ (crosses) and $Ni(CD_3COOD)^+$ (circles). The waveforms are simultaneously fit to a kinetic model which informs reaction mechanism and suggests dynamics. The resulting rate constants $k_{Ni(CH_3COOH)^+}$ = 0.2288 ± 0.0053 μs^{-1} and $k_{Ni(CD_3COOD)^+}$ = 0.0151 ± 0.0002 μs^{-1} represent the decay of a rate-determining reaction intermediate. Measurements and fits are normalized for clarity.

$$\begin{array}{l} \xrightarrow{k_{P_1}} P_1 \\ A \xrightarrow{k_{RL}} B \xrightarrow{k_{P_2}} P_2 \\ \xrightarrow{k_{P_3}} P_3 \end{array}$$

Scheme 1

simplistic kinetic model, P_1, P_2 and P_3 represent the three products, with ECFs determined by ratios of their respective dissociative rate constants k_{P_1}, k_{P_2} and k_{P_3}, and where a single rate-limiting step precedes reaction trifurcation. Based on Scheme 1, the rate law for each product P_i can be expressed in terms of the rate constants as:

$$\frac{d[P_i]}{dt} = \frac{[A]_0 k_{RL} k_{P_i}}{\sum_i k_{P_i} - k_{RL}} \left(e^{-k_{RL} t} - e^{-\sum_i k_{P_i} t} \right) \quad (2)$$

Integrating eqn (2) between $\tau + \alpha$ and $\tau + \alpha + \Delta$ limits obtains the SPIDRR response function for the τ-dependent product intensities S_{P_i}:

$$S_{P_i} = \frac{[A]_0 k_{RL} k_{P_i}}{\sum_i k_{P_i} - k_{RL}} \left(-\frac{1}{k_{RL}} e^{-k_{RL}(\tau+\alpha)} \left(e^{-k_{RL}\Delta} - 1 \right) + \frac{1}{\sum_i k_{P_i}} e^{-\sum_i k_{P_i}(\tau+\alpha)} \left(e^{-\sum_i k_{P_i}\Delta} - 1 \right) \right) \quad (3)$$

The SPIDRR measurements in Fig. 2, as well as all other SPIDRR measurements in this publication, have been fit to

eqn (3) to extract the rate-limiting rate constants. The resulting fits are shown in Fig. 2 as the black curves interpolating the measured data (colored circles and crosses), with the rate-limiting values of k reported in the caption. The agreement between the predictions of eqn (3) and the measurements of Fig. 2 is evident.

3.1.6 Reaction mechanism. A large KIE ($k^{RL}_{Ni(CH_3COOH)^+}/k^{RL}_{Ni(CD_3COOD)^+}$ or k_H/k_D) is manifest in Fig. 2 with magnitude = 15.2 ± 0.4. Large KIE magnitudes (≥15) are measured at all the laser energies used to initiate reactions in this study. A large KIE indicates that hydrogen transfer rate-limits the reaction and implicates hydrogen/deuterium QMT, which will be further discussed below. Given that decomposition of the $Ni(CH_3COOH)^+$ results in the formation of Ni^+ bound and free H_2O (green and blue traces of Fig. 1), we conclude that the rate-limiting step in Scheme 1 is the transfer of a methyl hydrogen to the acidic oxygen forming either $Ni(H_2O)^+$ in one dissociative pathway or neutral H_2O in another. Unexpectedly, since the formation of all three products is rate-limited by the decay of the same intermediate, then formation of the minor product, $Ni(CH_4O)^+$ + CO, must also be rate-limited by the methyl to acidic oxygen H-transfer despite having a structure whose formation does not require H-motion. These stoichiometric results, coupled with results from the reaction kinetics and photolysis experiments, suggest that the reaction must pass through a single tri-coordinate intermediate from which neutral and stable species are eliminated.

The most probable structure for this intermediate is a central Ni^+ cation bound to neutral CH_2, CO, and H_2O. This is considered a product complex (PC) which decays into the three observed products by elimination of neutral H_2O, C_2H_2O, and CO. The step that precedes formation of the PC requires the transfer of a methyl hydrogen to the acidic oxygen consistent with our kinetic results. It is the decay of this key intermediate forming this PC that controls reaction kinetics in this system. The important steps in the most probable reaction mechanism are shown in reaction (R2).

$$Ni(CH_3COOH)^+ \xrightarrow{h\nu} [Ni(CH_3)(CO)(OH)]^+$$
$$\xrightarrow{-C_2H_2O} Ni(H_2O)^+$$
$$\xrightarrow[\text{Rate Limiting}]{\text{H shift}} [Ni(CH_2)(CO)(H_2O)]^+ \xrightarrow{-CO} Ni(CH_4O)^+$$
$$\xrightarrow{-H_2O} Ni(C_2H_2O)^+ \quad \text{(R2)}$$

3.2 SPIDRR measurements of microcanonical rate constants

Fig. 3 (and Table SI-1) presents the microcanonical, rate-limiting rate constants, $k(E)$, extracted from SPIDRR measurements, performed at absorbed photon energies between 15 500 cm^{-1} (185.4 kJ mol^{-1}) and 19 800 cm^{-1} (236.9 kJ mol^{-1}). The rate

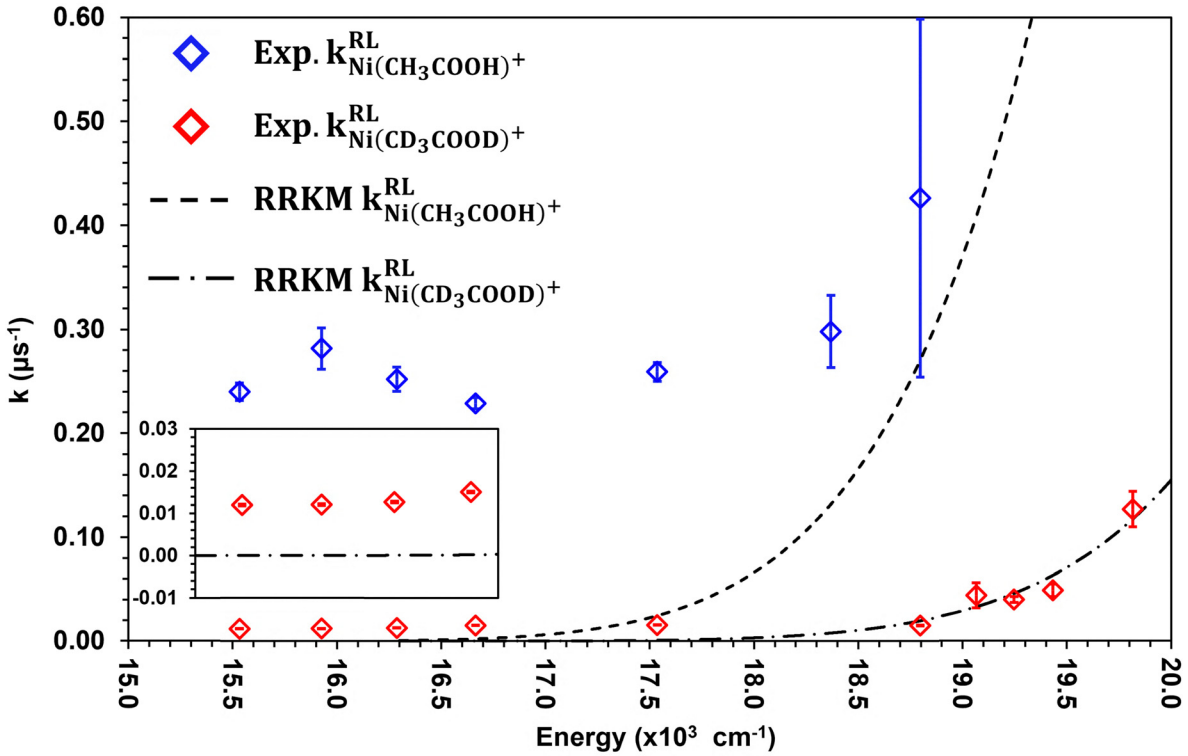

Fig. 3 Energy dependence of the unimolecular microcanonical rate constants $k(E)$, measured (blue and red diamonds) for the photon-initiated dissociative rearrangements of $Ni(CH_3COOH)^+$ and $Ni(CD_3COOD)^+$ and modeled with RRKM (dashed and dotted curves respectively), with WKB tunneling corrections calculated on the MEP pathway (Fig. 4). The inset shows the lower energy rate constants and RRKM modeling for the $Ni(CD_3COOD)^+$ isotopologue.

constants were determined through the simultaneous, unrestricted fitting of the three measured SPIDRR product formation waveforms to Scheme 1's kinetic model. The rate constant values were simultaneously optimized in a squared residual minimization routine from the predictions of eqn (3). This yielded four rate constants per absorbed photon energy for each isotopologue. The values of k_{P_1}–k_{P_3} yielded ratios consistent with the ECFs and were of such magnitude not to influence the reaction rates. The results of this analysis are the three solid curves in Fig. 2.

The rate-limiting rate constant $k(E)$ for the dissociation of $Ni(CD_3COOD)^+$ (red diamonds, Fig. 3) only slightly increases over a large (15 500–18 800 cm^{-1}) energy interval, retaining values of (0.010–0.015) μs^{-1} (see Fig. 3 inset). The reaction rate constants' energy dependence appears linear over this wide energy range with a near zero slope suggesting that the rate-limiting step in the rearrangement reaction is largely independent of system energy within this range. However, a significant 3× increase in k_{RL} is recorded once the $Ni(CD_3COOD)^+$ **RC** absorbs a 19 100 cm^{-1} quantum, an increase in the system's energy content of only 300 cm^{-1} from its previous measurement. Absorption of an additional 700 cm^{-1} of energy increases the reaction rate constant to 0.13 μs^{-1}, a factor of 10 increase over the linearly dependent rate constants measured at low-energy in this system (Fig. 3). Likewise, similar kinetic behavior is measured in the lighter $Ni(CH_3COOH)^+$ isotopologue (blue diamonds, Fig. 3). The rate constants near energy independent range extends from 15 500 cm^{-1} to 18 400 cm^{-1}, with the rate constants retaining values ~0.25 μs^{-1}. However, once the $Ni(CH_3COOH)^+$ absorbs an 18 800 cm^{-1} quantum, the rate-limiting reaction rate constant increases to 0.42 μs^{-1}, ~1.5× greater than its previous value. We acknowledge that this high-energy measurement in the $Ni(CH_3COOH)^+$ system has a larger error relative to other measurements as this rate constant's magnitude is approaching the upper limit to the dynamic range of our technique.

We consider the energies where the microcanonical rate constants' energy dependence rapidly increases, 18 800 cm^{-1} and 19 100 cm^{-1} for $Ni(CH_3COOH)^+$ and $Ni(CD_3COOD)^+$ respectively, as threshold values associated with a rapidly changing kinetic competition. We believe that the underlying reaction dynamics responsible for such thresholds is a central outcome of this study. Our interpretation of this system's reaction dynamics is presented in Section 4.

3.3 Computational results

The reaction mechanism was computationally studied using DFT as described in Section 2.2. The zero point energy (ZPE) corrected ground doublet PES is provided in Fig. 4. We define zero as the **RC** energy as the reaction begins here and continues

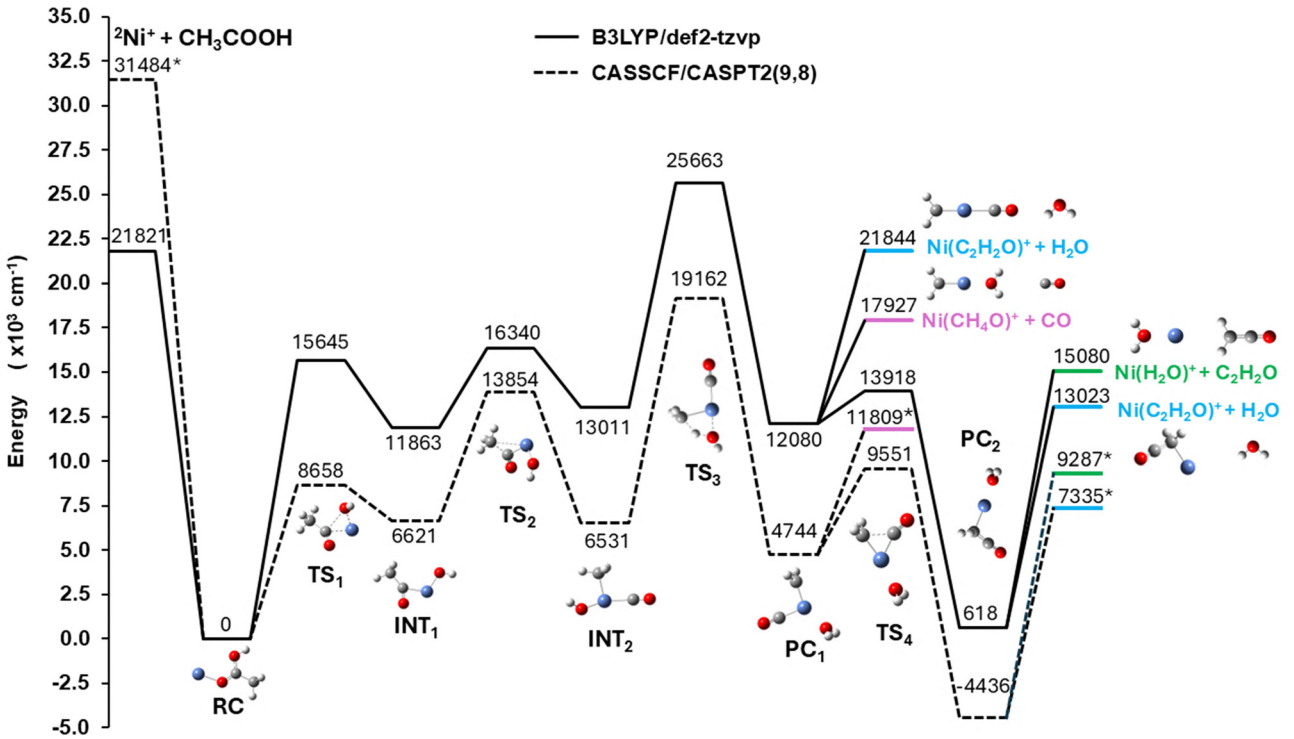

Fig. 4 PES for the titular reaction, complete with key intermediate (INT) and transition state (TS) structures and ZPE-corrected energies, optimized by DFT at B3LYP level with the def2-tzvp basis set (solid line). Single-point MRCI energy corrections on the stationary structures between **RC** and **PC_2** by CASSCF/CASPT2(9,8) are also shown (dashed line). MRCI energies representing sums of molecular energies are marked with an asterisk (*). They are calculated with different CASs than (9,8) as determined by RI-MP2 because of the different electron count. CH_3COOH energy is calculated with a (6,6) active space, Ni^+ ion energy with (5,9), H_2O with (4,4), CO with (6,4), and C_2H_2O with (6,6) active space. These are consistent with simple, neutral organic molecules having limited energy contributions from electronically excited states. A reproduction of Fig. 4 with reported energies converted to kJ mol^{-1} is included as Fig. SI-6.

to the right following photon absorption. The Ni^+ cation approaches **TS_1** and activates a C–OH bond to form the first reaction intermediate, **INT_1**. Activation of the C–CH_3 bond was computationally explored but resulted in a significantly larger barrier than **TS_1** and would therefore be uncompetitive in this reaction. The C–Ni–O bond rotates to form **TS_2** which brings the methyl group into proximity with the Ni atom.

Transfer of this methyl group onto the Ni atom results in the reaction's second intermediate, a tricoordinated Ni species, **INT_2**. The **INT_2** geometry places the OH and CH_3 functional groups at adjacent positions on the Ni atom with O–Ni–C bond angle of 149.55 degrees. The highest barrier in this reaction is **TS_3** which decreases the O–Ni–C bond angle to 76.58 degrees, facilitating the transfer of a methyl hydrogen onto the OH group. Intermediate 4 is the tricoordinated **PC_1** which binds neutral H_2O and CO to the Ni atom within a $Ni(CH_2)^+$ cation. Release of CO generates the minor $Ni(CH_4O)^+$ product and this product structure may be responsible for the observed $Ni(CH_2)^+$ photolysis product (see Fig. 1, Section 3.1.3). However, this pathway competes with a further rearrangement of **PC_1** into **PC_2** over **TS_4**. Carbon–carbon bond coupling between the CO group and the CH_2 carbenoid (**TS_4**) is favorable (13 918 cm^{-1}, 38.79 kcal mol^{-1}) relative to CO elimination (17 917 cm^{-1}, 51.23 kcal mol^{-1}). This leads to the formation of a second product complex (**PC_2**) from which dissociation of neutral species H_2O or C_2H_2O generates the final products. The calculated energy ordering of the products ($E_{Ni(C_2H_2O_2)^+} < E_{Ni(H_2O)^+} < E_{Ni(CH_4O)^+}$) is consistent with measured ECF yields.

The DFT calculated reaction pathway of Fig. 4 effectively reduces to an OA/RE sequence. However, despite experimental agreement with portions of the mechanism, the DFT energies appear only relatively correct. For example, the rate-limiting **TS_3** energy is far greater than the threshold energies measured in Fig. 3, and is even higher than the energy of the separated reactants. The ground state of open shell transition metals are often formed as a superposition of low energy, nearly degenerate states and are thus multiconfigurational. Single Slater determinant techniques, as DFT, often fail to describe the static electron correlation attributed to such systems. Thus, multireference methods were considered to better describe the measured chemistry.[81,84] Resolution-of-Identity Møller–Plesset second-order perturbation theory (RI-MP2) was employed as a diagnostic tool to determine whether nearly degenerate orbitals existed in the $Ni(CH_3COOH)^+$ system and thereby exhibit strong static electron correlation effects. Using MP2, 193 natural orbitals (NO) were generated and their occupation numbers determined. Three of these NOs displayed fractional occupation ($0 > n_e < 2$), contained considerable Ni 3d character (46–66%), and were delocalized onto the organic fragments. Fractional occupation of Ni 3d-like NOs indicates nearly degenerate states while the delocalization suggests contributions from the organic bonding partners. It was decided to employ CASSCF (complete active space self-consistent field) calculations and include both metal d and ligand p/π and π* orbitals in the active space.

All 193 MP2 orbitals were ranked by their deviation from the closed-shell limits. The eight orbitas with the largest deviations had obvious Ni 3d character and/or Ni–O (2p/π/π*) overlap. There were approximately 9 electrons in these eight NOs. Therefore, multireference CASSCF/CASPT2(9,8) single-point corrections were performed to capture both the static and dynamic correlation effects that single-reference DFT cannot.

The CASSCF/CASPT2(9,8) single-point energy corrections, calculated with the def2-TZVP basis set, were performed on the structures calculated by DFT between separated reactants and products, which reduced energy differences between the **RC** and each INT and TS structure (Fig. 4). Single-point corrections with a different active space were also performed on all other structures with a different electron count. The active spaces used therein are reported in the caption of Fig. 4. The CASSCF/CASPT2 corrected energy for the rate-determining H-transfer TS was reduced to 19 162 cm^{-1} (229.2 kJ mol^{-1}) above the **RC** level. This energy is still above our highest energy kinetic measurement for $Ni(CH_3COOH)^+$, but is also significantly lower than the DFT energy and as such the multireference calculations appear more consistent with observation.

4 Discussion

4.1 An *ad hoc* RRKM correction to the activation energy

We have previously observed $k(E)$ *vs.* E energy thresholds in the Co^+ mediated rearrangement reaction of several organic species.[59,60] In those studies, the measured threshold energies were interpreted as upper limits to the classical Eyring barrier energy. In a similar vein, we associate an 18 800 cm^{-1} energy as an upper limit to the H-transfer Eyring barrier energy in the $Ni(CH_3COOH)^+$ PES (**TS_3**, Fig. 4). Correspondingly, the measured 19 100 cm^{-1} threshold in the $Ni(CD_3COOD)^+$ system is due to the ZPE reduction attributed to deuterium substitution. The threshold energy difference, 300 cm^{-1}, is of sufficient magnitude to be a primary isotope effect consistent with a C–H stretch becoming imaginary at the H-transfer barrier. Thus, we interpret the energy thresholds in the measured rate constants energy dependence of Fig. 3 as the dynamic transition from primarily H/D QMT to over-barrier (statistical) kinetics. To refine this interpretation, and further our dynamical description of this reaction, we employ Rice–Ramsperger–Kassel–Marcus[87–89] (RRKM) theory to calculate microcanonical rate constants and their energy dependence.

RRKM theory calculates microcanonical rate constants from first principles by considering the statistical distribution from the reactant to the transition state manifold along the minimum energy pathway (MEP). The microcanonical rate constant is calculated from:

$$k(E) = \sigma \frac{N_{TS}(E)}{2\pi\hbar\rho(E)} \quad (4)$$

Here, σ is the symmetry factor for the reaction, $\rho(E)$ is the reactant's density of states at energy E and $N_{TS}(E)$ is the transition state number of states at energy E above the activation barrier, V_0, which is the ZPE-corrected energy difference between the TS and its preceding INT. At the reaction energy, it is assumed that internal rotation of the H_3C–Ni bond in **INT_2**

is practically free. The methyl hydrogens may therefore move in the reaction along 3 degenerate paths, such that σ has a value of 3. For V_0, the **TS$_3$** energy is initially fixed at its calculated value, as opposed to a variational treatment which minimizes the reaction rate by optimizing the location of the surface that divides reactant from product. This is a standard approach and while variational effects may slightly influence the modeled reaction rates, this treatment is not expected to impact the conclusions of this study. In this work, only vibrational contributions to the density and number of states are considered with vibrational frequencies computed at the DFT level. Ignoring rotational contributions is an often-applicable approximation, particularly for large systems with small rotational constants. $N_{TS}(E)$ was calculated from the vibrational frequencies of the H-transfer transition state by numerical integration of the tunneling-corrected $\rho_{TS}(E)$, determined by direct count with the Beyer–Swinehart[90] algorithm. As reviewed by Richardson,[91] the cumulative sum of the Heaviside step function counting the states can be rewritten as an integral over the energy in the reaction coordinate E_{rxn} where $\rho_{TS}(E - E_{rxn}) = \sum_n \delta(E - \epsilon_n - E_{rxn})$. This allows the inclusion of the barrier transmission probability term $P(E_{rxn})$, as per Miller.[92,93]

$$N(E) = \sum_n \theta(E - \epsilon_n - V_0) = \int_0^E \rho_{TS}(E - E_{rxn}) P(E_{rxn}) \mathrm{d}E_{rxn} \quad (5)$$

The transmission probability $P(E_{rxn})$ is classically 0 for $E_{rxn} < V_0$ and 1 for $E_{rxn} > V_0$, but tunneling calculations of barrier penetration can replace the classical expression of $P(E_{rxn})$ to calculate tunneling corrections to the microcanonical RRKM determination of $k(E)$.

For this work, the energy-dependent tunneling probability is calculated using the Wentzel–Kramers–Brillouin (WKB) method,[71,72] as well as SCT[73–75] and LCT.[75–80] These tunneling corrections require the calculation of the MEP of the H-transfer barrier over **TS$_3$**. The MEP is first determined by DFT and then energy-corrected using MRCI along the intrinsic reaction coordinate (IRC) (Fig. SI-7). Eqn (6) and (7) briefly review how the WKB barrier penetration probability is calculated. SCT and LCT probabilities were computed from equations provided in Truhlar's work.[94]

$$P(E) = \left(1 + e^{\frac{2W(E)}{\hbar}}\right)^{-1} \quad (6)$$

$$W(E) = \begin{cases} \int_{x_i}^{x_f} \sqrt{2\mu[V(x) - E]}\mathrm{d}x & \text{for } E < V_0 \\ \frac{2\pi}{\omega_b}(V_0 - E) & \text{for } E > V_0 \end{cases} \quad (7)$$

Here, $V(x)$ is the potential energy as a function of the IRC (x, Å) in Fig. SI-7, x_i and x_f are the IRC turning points at energy E, and ω_b is the imaginary frequency of the vibrational mode associated with the TS.

Calculations of RRKM rate constants from eqn (4)–(7) were performed with a V_0 value of 12 631 cm^{-1}, which is the calculated **TS$_3$–INT$_2$** energy difference from Fig. 4. The **INT$_2$** energy is 6531 cm^{-1} above the **RC** energy. The calculated rate constants are plotted against the total energy of the system yielding their energy dependence. However, the resulting $k(E)$ curves did not match experimental results, and a 3600 cm^{-1} *ad hoc* reduction was applied to the system's total energy to bring agreement between experimental and modeled rates. This value was determined through visual optimization of the tunneling-corrected RRKM rate constants with the five high-energy rate constants measured in the Ni(CD$_3$COOD)$^+$ system. The correction is applied to both isotopologues but was intentionally determined using the heavier deuterium labeled species as this system's rate constants are less influenced by QMT. This *ad hoc* energy correction effectively raises the reaction's zero energy thereby reducing the calculated energy differences between the reaction's EC and INT and TS structures, preserving the energy ordering evident in Fig. 4. The energy dependence of the energy shifted, tunneling-corrected RRKM rate constants (dash and dash/dot lines, Fig. 3) exhibits the familiar ascending trend as the TS vibrational state density increases with energy and matches well the high-energy experimental observations of Fig. 3.

Although this 3600 cm^{-1} offset correction is substantial, it falls within the error range observed in CASPT2 treatments of open-shell transition-metal systems, particularly those with strong multiconfigurational character. Benchmark studies[95,96] have identified barrier discrepancies of 1700–2800 cm^{-1} (20–33 kJ mol^{-1}) between CASPT2 and higher-level methods such as CCSD(T) or MRCI+Q in comparable systems. These systematic deviations often stem from incomplete recovery of dynamic correlation, insufficient active-space size and neglect of scalar relativistic effects. Given these considerations, we applied a uniform 3600 cm^{-1} *ad hoc* shift to align the computed PES with experimental high-energy data, preserving relative energy ordering and kinetic trends while acknowledging the known limitations of CASPT2 for complex transition-metal systems.

Fig. 3 shows that the agreement between the final five measured Ni(CD$_3$COOD)$^+$ rearrangement rate constants with the energy-shifted, WKB-tunneling corrected RRKM rate constants is quite good. However, as the system's energy is reduced, the density of states at the TS reduces significantly, and the calculated rate constant profile quickly approaches zero. Despite the application of a tunneling correction to the RRKM theory, the calculated rate constants disagree with the observed Ni(CD$_3$COOD)$^+$ rearrangement rate constants as the system's energy is reduced (Fig. 3 inset). This disagreement between the calculated and observed rate constants is even more evident in the Ni(CH$_3$COOH)$^+$ system (blue symbols and curves, Fig. 3). Here, the tunneling corrected RRKM rate constant's energy dependence disagrees with observation at all energies. Incorporating SCT and LCT tunneling probabilities (Fig. SI-8) into eqn (5)–(7) extends tunneling rate constants to lower energies (Fig. SI-9) but also fails to describe the near energy independence of the measured rate constants. We believe that the discrepancies evident in Fig. 3 and Fig. SI-9

between the calculated and observed rate constant energy dependence are due to hydrogen tunneling that is not accounted for by the tunneling corrections herein applied (WKB, SCT and LCT, see SI-8). We believe that QMT is made far more efficient by Ni metal's electronic structure and its associated bonding as described below.

4.2 Quantum mechanical tunneling

As reported in Fig. 2, the formation rate of the products $Ni(H_2O)^+$, $Ni(CH_4O)^+$ and $Ni(C_2H_2O)^+$ is much greater than that of their corresponding heavier isotopologues. We observe an average KIE of 19 ± 3 throughout our lower-energy (15 500–18 500 cm^{-1}) measurements. KIE measurements above 2 generally indicate that the rate-limiting motion of a reaction is directly affected by isotopic labeling and is considered a primary KIE.[97] This indicates that C–H bond activation and its subsequent H-transfer rate limit this reaction, consistent with the calculated PES of Fig. 4.

High KIE values (>10) are generally ascribed to contributions from H/D QMT. Large H/D QMT KIEs are caused by the decreased tunneling efficiency of the heavier deuterium atom, with predicted QMT KIE magnitudes provided in Fig. SI-10. Although low KIE values have been proven possible in tunneling systems,[59,98] the large KIE measured here remains an indicator of rate limiting H/D QMT in the decomposition of $Ni(CH_3COOH)^+$ and its deuterated isotopologue. The high KIE measured in this system suggests that H-tunneling contributes significantly to the rate constants measured at low-energies.

Microcanonical rate constants for the Ni^+ induced rearrangement reaction are measured over the 15 000–20 000 cm^{-1} range in this study as seen in Fig. 3. Within this energy window, the reaction dynamics are changing from primarily quantum to primarily statistical reaction control. This is manifest as a competition in reaction kinetics that changes from slow to fast reaction rates. At low energy, H/D QMT is the primary contributor to the measured rate constants ($\sim$0.24 μs^{-1} and $\sim$0.01 μs^{-1} for H4 and D4 variants respectively), and this continues until the energy threshold is met. At threshold, the density of states at the TS becomes significant and the contributions from RRKM statistics cause the observed rapid increase in reaction rate constants: within a few hundred cm^{-1}, k_{RL} for the H4 isotopologue almost doubles, and triples for the D4 isotopologue. Thus, the threshold is the energy at which over-the-barrier kinetic rates, described by RRKM statistics, outcompete QMT. This threshold is estimated as 18 800 cm^{-1} for $Ni(CH_3COOH)^+$, and 19 100 cm^{-1} for $Ni(CD_3COOD)^+$.

We conclude that H/D QMT contributes substantially to the low-energy reaction rates measured in this study. Evidence of this is provided by the large measured KIE, the threshold values which are interpreted as the energies where the reaction dynamics change from primarily QMT to statistical, and the agreement between the higher energy rate constants' measured energy dependence with the calculated RRKM rate constants' energy dependence in Fig. 3. This interpretation concludes that: (i) the low-energy rate constants measured in this study result from QMT with negligible contributions from statistics, (ii) the H/D QMT energy dependence is not described by MEP-based tunneling corrections (WKB, SCT, LCT) but rather appears to linearly, monotonically decrease with decreasing energy, and (iii) the nearly pure QMT rate constants extrapolate to energies far lower than the lowest energy measurement of Fig. 3. The findings of this study indicate that C–H bond activation occurs at low energies by quantum mechanical means while retaining high reaction turnovers (k_{HT} = 0.25 μs^{-1} = 250 000 s^{-1}). These surprising tunneling behaviors demand further consideration.

4.3 Surprising tunneling behaviors

This is our third publication where we have presented near energy independent rate constants, and to the best of our knowledge, we are the only group who have measured this unusual feature in a microcanonical study. Canonical studies have commonly measured rate constants that are nearly temperature independent when the reaction occurs at cryogenic temperatures. Although several groups have made such measurements,[99,100] we focus on a cryogenic study of QMT H-diffusion on a solid nickel surface where the authors have observed two different temperature dependencies.[101,102] In a similar vein to our interpretation of Fig. 3, the authors and others interpreted the temperature dependencies in their measured diffusion coefficients as a transition from primarily QMT to over-barrier Arrhenius behavior.[103] The temperature independence observed in each of these cryogenic rate studies is understood to result from deep tunneling originating in an unchanging quantum state distribution. An unchanging quantum state distribution cannot be ascribed to the $Ni^+(CH_3COOH)$ system studied here, however, as described in the procedure section, due to the high density of states and the fast (ns scale) IVR processes occurring following photon absorption. Should the reaction occur along the excited PES, then there may be a relatively constant distribution of quantum states within the excited electronic state, that is responsible for the rate constants near energy independence observed in Fig. 3. However, the entropy-driven internal conversion and strong electronic couplings between the excited and ground doublet states make this highly improbable. As such, the tunneling behaviors identified in Fig. 3 cannot be explained by a localized quantum state distribution as was used to explain temperature-independent tunneling rates of systems within cryogenically cold environments.

Thus, we turn to modern tunneling theories where alternate pathways are followed by the tunneling particle at energies below the barrier. It is well known that below the classical Eyring barrier, the reaction is not bound to proceed through the pathway defined by the MEP as predicted by statistical transition state theory. Rather, reactive conformations may be sampled that exhibit higher energy barriers than the TS, but for which the barrier shape is more favorable to tunneling. This phenomenon is dubbed "corner cutting",[76] and SCT and LCT are two common approaches to corner cutting in which curvature is used to describe deviations from the MEP. In SCT, a small deviation from the MEP is taken into consideration

by adjusting the effective tunneling mass through a correction that considers the coupling of vibrational modes orthogonal to the IRC. In LCT, the tunneling pathway is the straight-line path from the reactant to the product conformations at each system energy. Both theories rely on the determination of the MEP, Hessian matrices, and geometries along this pathway. As reaction energy is increased, both LCT and SCT converge to follow the MEP. Microcanonical tunneling probabilities calculated with SCT and LCT are presented in Fig. SI-8 and are implemented into eqn (4)–(7) to determine rate constants. Fig. SI-9 presents these calculated rate constants, which fail to describe the observations of this study.

We believe that the unique tunneling properties measured here and in our earlier Co^+ mediated reaction studies are due to the electronic character of the transition metal. We have previously demonstrated that a very narrow barrier width could account for the very efficient H/D QMT measured during the Co^+ mediated decomposition of CH_3COOH. We propose that key TS structures along the PES place organic fragments in proximity such that transfer distances are reduced, thereby making QMT efficient. This is consistent with eqn (6) and (7) which show that the QMT probability has a greater dependence on barrier width relative to particle mass or system energy deficiency. To this end, we have searched for low-energy structures that may contribute to QMT by reducing the hydrogen transfer distance between **INT$_2$** and **PC$_1$**.

We performed a relaxed scan of the relevant bond angles and bond lengths around the transferring hydrogen. Specifically, we varied the O–Ni–C bond angle and the H–Ni, C–H, and O–H bond distances, where the hydrogen in question originates from the methyl group adjacent to the nickel center. We thus located a bridging structure, presented in Fig. 5 as the **Bridge**. This structure is a second order saddle point on the PES with a ZPE corrected energy of 30 224 cm^{-1} (361.6 kJ mol^{-1}) at the B3LYP/def2-TZVP level. Application of CASSCF-CASPT2(9,8), utilizing this same def2-TZVP basis set, reduces this energy to 22 555 cm^{-1} (269.8 kJ mol^{-1}), which is 3393 cm^{-1} (40.6 kJ mol^{-1}) above **TS$_3$** (see Fig. 4).

In the **Bridge**, the transferring hydrogen becomes transiently coordinated to the nickel atom. The hydrogen here appears to form a three-center interaction between the methyl carbon, nickel center, and the Ni-bound oxygen atom. This geometry represents a pre-reactive configuration, distinct from the transition state, where the hydrogen is not fully transferred to oxygen but instead shows partial bonding to both Ni and the leaving group. The comparison with the original transition state structure reveals that in the transition state, the hydrogen is already positioned between the methyl carbon and the oxygen atom, with no direct interaction with nickel. However, in the newly located **Bridge** geometry, the hydrogen clearly moves toward the Ni center, suggesting a potential Ni–H agostic interaction or incipient Ni–H bond formation which facilitates C–H bond activation.

This H shift from a C–H to a Ni–H bond displaces the hydrogen atom only 6 pm from its previous position on the methyl group. This finding supports the idea that during hydrogen transfer, nickel may stabilize the migrating hydrogen (or deuterium), forming a transient structure that facilitates the tunneling process by reducing the C–H bond activation barrier width. It also highlights the flexibility of the metal center in accommodating the H during bond reorganization. We believe that the **Bridge** and similar species have the appropriate structure, bonding, and energy to participate in Ni-enhanced corner cutting tunneling pathways, similar to LCT but extending their contributions to higher energy ranges.

Assuming that structures such as the Ni–H bridge are part of the multidimensional tunneling pathways available on the PES, then the activation of a high energy C–H bond is effectively complete following a 6 pm hydrogen displacement. This represents a very narrow barrier that will significantly enhance QMT probability. In fact, we have previously demonstrated[59] that the application of a very simple tunneling theory to very narrow barriers yields tunneling probabilities that are nearly energy independent, as observed previously as well as in Fig. 3 of this study. Thus, we propose that the electronic structure and

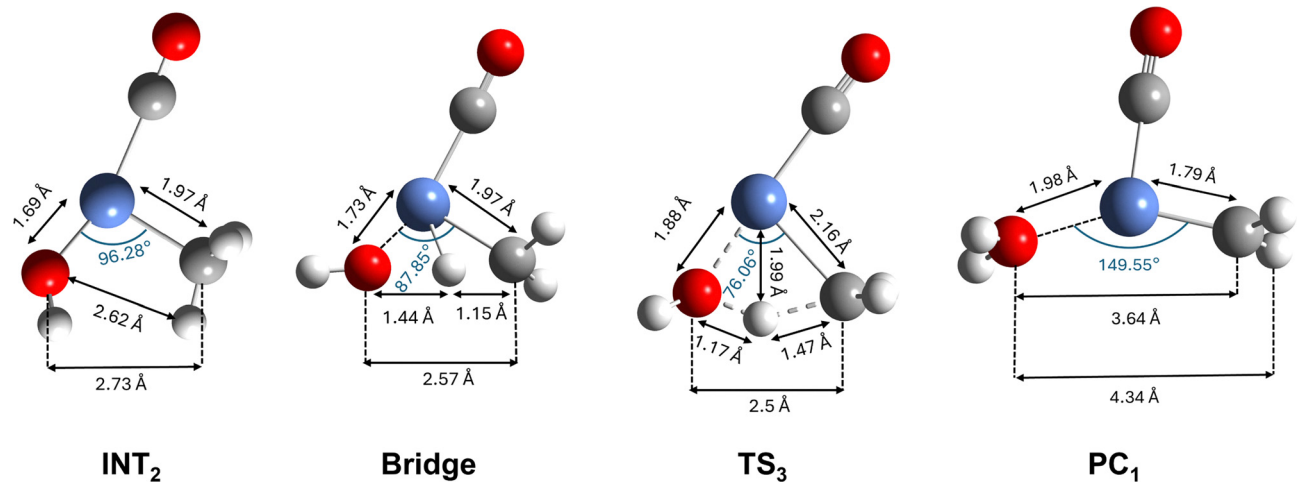

Fig. 5 Geometries, bond distances and angles for the **INT$_2$**, **TS$_3$** and **PC$_1$** structures along the MEP, as well as the high-energy "**Bridge**" structure involving a transitory Ni–H bond.

consequent bonding interactions of the transition metal are key to efficient QMT and are responsible for the large deviation between experimental findings from the tunneling-corrected RRKM models. Moreover, motion away from the MEP, and exploration of the multidimensional PES may lead to structures such as the Ni–H Bridge which may be accessed in below-barrier dynamics to facilitate QMT.

5 Conclusions

An experimental investigation into the kinetic properties of the Ni^+ reaction with CH_3COOH and its perdeuterated analog, CD_3COOD, has been presented and complemented with theory. Formation kinetics of three products are followed over a range of system internal energies. The reaction mechanism is deduced as an OA/RE sequence rate limited by a methyl C–H activation and hydrogen transfer to the OH moiety. Microcanonical rate constants are measured over a range of several thousand wavenumbers revealing a threshold region as realized by a rapid increase in reaction rate constant values over a small energy window. This is interpreted as an upper limit to the hydrogen transfer Eyring barrier. Rate constants calculated by RRKM theory are fit to this measured threshold (*i.e.* with an *ad hoc* correction to the CASSCF energy), and estimate this rate-limiting Eyring barrier at 15 560 cm^{-1} above the **RC** energy.

Measurements of rate constants extend far below the threshold, with magnitudes too large to be accounted for by RRKM theory. We interpret these rate constants as containing significant contributions from H/D QMT. This interpretation is supported by the high KIE ($\sim$15–20) measured in this low-energy regime, as well as the shift between threshold energies measured in the two isotopologues, which is consistent with a primary KIE. These nearly pure H/D tunneling rate constants exhibit two surprising behaviors. First, the rate constants are nearly energy independent, showing a slight monotonic increase over the measured energy range. Second, it appears that the tunneling range will extrapolate to very low energies. These curious behaviors cannot be attributed to QMT that follows a pathway below the classically described MEP across the rate-limiting TS, and moreover, modern corner-cutting theories like SCT and LCT also fail to replicate our observation.

Instead, we propose that the Ni^+ electronic structure may promote QMT, where the bonding schemes in key structures place organic fragments in a proximity that facilitates H/D transfer. Such structures are proposed to exist along the multidimensional PES, providing tunneling pathways distinct from the MEP with reduced barrier width and consequent energy dependence. We employed multireference calculations and have identified a representative candidate structure which is a second order saddle point on the PES. We propose that this structure illustrates our hypothesis by participating as a bridge for hydrogen tunneling. It features a Ni–H transient bond formed following C–H activation that requires a hydrogen motion of only 6 pm. We propose to continue testing our metal promoted QMT hypothesis in future studies of other transition metals as well as performing instanton calculations to better identify potential tunneling paths.

We have confidence that the QMT-facilitating behavior of Ni^+, which we also measured for Co^+, is a contributor to the metal's versatility in C–H bond activation reactions which may extend to very low energies. Findings that spring from gas-phase kinetic experiments underscore how significant such studies are towards advancing fundamental insight and understanding the properties of transition metals. Comprehending and elucidating such will forward catalyst design and development, especially as it pertains to heterogeneous catalysis on surfaces, nanoparticles, and single-atom catalysts.

Conflicts of interest

There are no conflicts to declare.

Data availability

Data for this article, in the form of the raw data files secured from our instrument, as well as Gaussian and ORCA output files, are available at Texas Data Repository, at **https://dataverse.tdl.org/dataverse/Bellert**.

Supplementary information is available. See DOI: **https://doi.org/10.1039/d5cp02626a**.

Acknowledgements

Acknowledgement is made to the donors of The American Chemical Society Petroleum Research Fund for support (or partial support) of this research.

References

1 Y. Ziyan, C. Rongzhen, Z. Ling, L. Yuhang and L. Chunzhong, Recent Progress in Nickel Single-Atom Catalysts for the Electroreduction of CO_2 to CO, *Ind. Chem. Mater.*, 2024, **2**(4), 533–555, DOI: **10.1039/D3IM00109A**.

2 Z. Zhang, C. Shen, K. Sun, X. Jia, J. Ye and C. J. Liu, Advances in Studies of the Structural Effects of Supported Ni Catalysts for CO_2 Hydrogenation: From Nanoparticle to Single Atom Catalyst, *J. Mater. Chem. A*, 2022, **10**(11), 5792–5812, DOI: **10.1039/D1TA09914K**.

3 W. Liu, Y. Chen, H. Qi, L. Zhang, W. Yan, X. Liu, X. Yang, S. Miao, W. Wang, C. Liu, A. Wang, J. Li and T. Zhang, A Durable Nickel Single-Atom Catalyst for Hydrogenation Reactions and Cellulose Valorization under Harsh Conditions, *Angew. Chem., Int. Ed.*, 2018, **57**(24), 7071–7075, DOI: **10.1002/ANIE.201802231**.

4 N. Dong, T. Roman and C. Stampfl, Nickel-Based Single-Atom Alloys for Methane Dehydrogenation and the Effect of Subsurface Carbon: First-Principles Investigations, *Catalysts*, 2024, **14**(2), 145, DOI: **10.3390/CATAL14020145**.

5 A. D. Nishchakova, L. G. Bulusheva and D. A. Bulushev, Supported Ni Single-Atom Catalysts: Synthesis, Structure,

and Applications in Thermocatalytic Reactions, *Catalysts*, 2023, **13**(5), 845, DOI: 10.3390/CATAL13050845.

6 M. Akri, A. El Kasmi, C. Batiot-Dupeyrat and B. Qiao, Highly Active and Carbon-Resistant Nickel Single-Atom Catalysts for Methane Dry Reforming, *Catalysts*, 2020, **10**(6), 630, DOI: 10.3390/CATAL10060630.

7 M. B. Gawande, K. Ariga and Y. Yamauchi, Single-Atom Catalysts, *Adv. Mater. Interfaces*, 2021, **8**(8), 2100436, DOI: 10.1002/ADMI.202100436.

8 Z. Li, B. Li and C. Yu, Dynamic Catalytic Structures of Single-Atom (or Cluster) Catalysts: A Perspective Review, *Small Struct.*, 2025, **6**(5), 2400479, DOI: 10.1002/SSTR.202400479.

9 S. K. Kaiser, Z. Chen, D. Faust Akl, S. Mitchell and J. Pérez-Ramírez, Single-Atom Catalysts across the Periodic Table, *Chem. Rev.*, 2020, **120**(21), 11703–11809, DOI: 10.1021/ACS.CHEMREV.0C00576.

10 Z. Ma, V. G. Chandrashekhar, B. Zhou, A. M. Alenad, N. Rockstroh, S. Bartling, M. Beller and R. V. Jagadeesh, Stable and Reusable Ni-Based Nanoparticles for General and Selective Hydrogenation of Nitriles to Amines, *Chem. Sci.*, 2022, **13**(36), 10914–10922, DOI: 10.1039/D2SC02961H.

11 Z. Yuan, X. Li, G. Wang, Z. Zhu, Y. Liao, Z. Zhang and B. Liu, Efficient Hydrogenation of N-Heteroarenes into N-Heterocycles over MOF-Derived CeO_2 Supported Nickel Nanoparticles, *Mol. Catal.*, 2023, **540**, DOI: 10.1016/J.MCAT.2023.113052.

12 A. Pérez Alonso, S. Mauriés, J. B. Ledeuil, L. Madec, D. Pham Minh, D. Pla and M. Gómez, Nickel Nanoparticles Immobilized on Pristine Halloysite: An Outstanding Catalyst for Hydrogenation Processes, *ChemCatChem*, 2022, **14**(22), DOI: 10.1002/CCTC.202200775.

13 F. Alonso, P. Riente and M. Yus, Nickel Nanoparticles in Hydrogen Transfer Reactions, *Acc. Chem. Res.*, 2011, **44**(5), 379–391, DOI: 10.1021/AR1001582.

14 I. Buslov, F. Song and X. Hu, An Easily Accessed Nickel Nanoparticle Catalyst for Alkene Hydrosilylation with Tertiary Silanes, *Angew. Chem., Int. Ed.*, 2016, **55**(40), 12295–12299, DOI: 10.1002/ANIE.201606832.

15 I. Ahmad, H. Alothaid, M. M. Habibullah, T. H. Wani and S. Ikram, Deciphering the Catalytic Activity of Nickel Anchored on Fe_3O_4@SiO_2@3-CPMS@L as a Magnetically Recoverable Nanocatalyst for the Efficacious Reduction of 4-Nitrophenol, Nitrobenzene, and Methyl Orange, *J. Environ. Manage.*, 2024, 367, DOI: 10.1016/j.jenvman.2024.121795.

16 S. Payamifar, A. Foroozandeh, M. Abdouss and A. Poursattar Marjani, Magnetic Nickel Nanoparticle Catalyst on β-Cyclodextrin-Modified Fe_3O_4 for Nitroarene Hydrogenation, *Sci. Rep.*, 2024, **14**(1), 28493, DOI: 10.1038/S41598-024-79709-0.

17 J. Wang, W. Li, H. Wang, A. T. Ogunbiyi, X. Dou and Q. Ma, Effects of the Novel Catalyst Ni-S2O8 2-K_2O/TiO_2 on Efficient Lignin Depolymerization, *RSC Adv.*, 2020, **10**(14), 8558–8567, DOI: 10.1039/c9ra10675h.

18 M. Hosseini-Sarvari and A. Dehghani, Nickel/TiO_2-Catalyzed Suzuki–Miyaura Cross-Coupling of Arylboronic Acids with Aryl Halides in MeOH/H_2O, *Monatsh. Chem.*, 2023, **154**(3–4), 397–405, DOI: 10.1007/S00706-023-03052-9.

19 S. D. Ittel, L. K. Johnson and M. Brookhart, Late-Metal Catalysts for Ethylene Homo- and Copolymerization, *Chem. Rev.*, 2000, **100**(4), 1169–1203, DOI: 10.1021/CR9804644.

20 M. R. Kesti, G. W. Coates and R. M. Waymouth, Homogeneous Ziegler-Natta Polymerization of Functionalized Monomers Catalyzed by Cationic Group IV Metallocenes, *J. Am. Chem. Soc.*, 1992, **114**(24), 9679–9680, DOI: 10.1021/JA00050A069.

21 S. Abate, K. Barbera, E. Giglio, F. Deorsola, S. Bensaid, S. Perathoner, R. Pirone and G. Centi, Synthesis, Characterization, and Activity Pattern of Ni–Al Hydrotalcite Catalysts in CO_2 Methanation, *Ind. Eng. Chem. Res.*, 2016, **55**(30), 8299–8308, DOI: 10.1021/ACS.IECR.6B01581.

22 H. Mu, L. Pan, D. Song and Y. Li, Neutral Nickel Catalysts for Olefin Homo- and Copolymerization: Relationships between Catalyst Structures and Catalytic Properties, *Chem. Rev.*, 2015, **115**(22), 12091–12137, DOI: 10.1021/CR500370F.

23 L. K. Johnson, C. M. Killian and M. Brookhart, New Pd(II)- and Ni(II)-Based Catalysts for Polymerization of Ethylene and α-Olefins, *J. Am. Chem. Soc.*, 1995, **117**(23), 6414–6415, DOI: 10.1021/JA00128A054.

24 R. M. Stolley, M. T. Maczka and J. Louie, Nickel-Catalyzed [2+2+2] Cycloaddition of Diynes and Cyanamides, *Eur. J. Org. Chem.*, 2011, (20–21), 3815–3824, DOI: 10.1002/EJOC.201100428.

25 R. M. Stolley, M. T. MacZka and J. Louie, Nickel-Catalyzed [2+2+2] Cycloaddition of Diynes and Cyanamides, *Eur. J. Org. Chem.*, 2011, (20–21), 3815–3824, DOI: 10.1002/EJOC.201100428.

26 J. Louie, J. E. Gibby, M. V. Farnworth and T. N. Tekavec, Efficient Nickel-Catalyzed [2+2+2] Cycloaddition of CO_2 and Diynes, *J. Am. Chem. Soc.*, 2002, **124**(51), 15188–15189, DOI: 10.1021/JA027438E.

27 T. N. Tekavec, A. M. Arif and J. Louie, Regioselectivity in Nickel(0) Catalyzed Cycloadditions of Carbon Dioxide with Diynes, *Tetrahedron*, 2004, **60**(34), 7431–7437, DOI: 10.1016/J.TET.2004.06.025.

28 T. N. Tekevac and J. Louie, Nickel-Catalyzed Cycloaddition of Unsaturated Hydrocarbons and Carbonyl Compounds, *Org. Lett.*, 2005, **7**(18), 4037–4039, DOI: 10.1021/OL0515558.

29 P. R. Chopade and J. Louie, [2+2+2] Cycloaddition Reactions Catalyzed by Transition Metal Complexes, *Adv. Synth. Catal.*, 2006, **348**(16–17), 2307–2327, DOI: 10.1002/ADSC.200600325.

30 T. Tsuda, S. Morikawa, R. Sumiya and T. Saegusa, Nickel(0)-Catalyzed Cycloaddition of Diynes and Carbon Dioxide to Bicyclic α-Pyrones, *J. Org. Chem.*, 1988, **53**(14), 3140–3145, DOI: 10.1021/JO00249A003.

31 T. N. Tekavec and J. Louie, Nickel-Catalyzed Cycloadditions of Unsaturated Hydrocarbons, Aldehydes, and Ketones, *J. Org. Chem.*, 2008, **73**(7), 2641–2648, DOI: 10.1021/JO702508W.

32 H. Zhu, R. Razzaq, C. Li, Y. Muhmmad and S. Zhang, Catalytic Methanation of Carbon Dioxide by Active Oxygen

Material $Ce_xZr_{1-x}O_2$ Supported Ni–Co Bimetallic Nanocatalysts, *AIChE J.*, 2013, **59**(7), 2567–2576, DOI: 10.1002/AIC.14026.

33 H. Liu, X. Zou, X. Wang, X. Lu and W. Ding, Effect of CeO_2 Addition on Ni/Al_2O_3 Catalysts for Methanation of Carbon Dioxide with Hydrogen, *J. Nat. Gas Chem.*, 2012, **21**(6), 703–707, DOI: 10.1016/S1003-9953(11)60422-2.

34 P. A. U. Aldana, F. Ocampo, K. Kobl, B. Louis, F. Thibault-Starzyk, M. Daturi, P. Bazin, S. Thomas and A. C. Roger, Catalytic CO_2 Valorization into CH_4 on Ni-Based Ceria-Zirconia. Reaction Mechanism by Operando IR Spectroscopy, *Catal. Today*, 2013, **215**, 201–207, DOI: 10.1016/J.CATTOD.2013.02.019.

35 J. Martínez, E. Hernández, S. Alfaro, R. L. Medina, G. V. Aguilar, E. Albiter and M. A. Valenzuela, High Selectivity and Stability of Nickel Catalysts for CO_2 Methanation: Support Effects, *Catalysts*, 2019, **9**(1), 24, DOI: 10.3390/CATAL9010024.

36 W. Zhen, B. Li, G. Lu and J. Ma, Enhancing Catalytic Activity and Stability for CO_2 Methanation on Ni@MOF-5 via Control of Active Species Dispersion, *Chem. Commun.*, 2015, **51**(9), 1728–1731, DOI: 10.1039/C4CC08733J.

37 J. Ren, X. Qin, J. Z. Yang, Z. F. Qin, H. L. Guo, J. Y. Lin and Z. Li, Methanation of Carbon Dioxide over Ni–M/ZrO_2 (M = Fe, Co, Cu) Catalysts: Effect of Addition of a Second Metal, *Fuel Process. Technol.*, 2015, **137**, 204–211, DOI: 10.1016/J.FUPROC.2015.04.022.

38 F. Ocampo, B. Louis and A. C. Roger, Methanation of Carbon Dioxide over Nickel-Based $Ce_{0.72}Zr_{0.28}O_2$ Mixed Oxide Catalysts Prepared by Sol–Gel Method, *Appl. Catal., A*, 2009, **369**(1–2), 90–96, DOI: 10.1016/J.APCATA.2009.09.005.

39 H. Ochiai, M. Jang, K. Hirano, H. Yorimitsu and K. Oshima, Nickel-Catalyzed Carboxylation of Organozinc Reagents with CO_2, *Org. Lett.*, 2008, **10**(13), 2681–2683, DOI: 10.1021/OL800764U.

40 Y. Makida, E. Marelli, A. M. Z. Slawin and S. P. Nolan, Nickel-Catalysed Carboxylation of Organoboronates, *Chem. Commun.*, 2014, **50**(59), 8010–8013, DOI: 10.1039/C4CC03650F.

41 N. Huguet, I. Jevtovikj, A. Gordillo, M. L. Lejkowski, R. Lindner, M. Bru, A. Y. Khalimon, F. Rominger, S. A. Schunk, P. Hofmann and M. Limbach, Nickel-Catalyzed Direct Carboxylation of Olefins with CO_2: One-Pot Synthesis of α,B-Unsaturated Carboxylic Acid Salts, *Chem. – Eur. J.*, 2014, **20**(51), 16858–16862, DOI: 10.1002/CHEM.201405528.

42 Y. G. Chen, X. T. Xu, K. Zhang, Y. Q. Li, L. P. Zhang, P. Fang and T. S. Mei, Transition-Metal-Catalyzed Carboxylation of Organic Halides and Their Surrogates with Carbon Dioxide, *Synthesis*, 2018, (1), 35–48, DOI: 10.1055/S-0036-1590908.

43 J. Davies, D. Janssen-Müller, D. P. Zimin, C. S. Day, T. Yanagi, J. Elfert and R. Martin, Ni-Catalyzed Carboxylation of Aziridines En Route to β-Amino Acids, *J. Am. Chem. Soc.*, 2021, **143**(13), 4949–4954, DOI: 10.1021/JACS.1C01916.

44 K. L. Jensen, E. A. Standley and T. F. Jamison, Highly Regioselective Nickel-Catalyzed Cross-Coupling of *N*-Tosylaziridines and Alkylzinc Reagents, *J. Am. Chem. Soc.*, 2014, **136**(31), 11145–11152, DOI: 10.1021/JA505823S.

45 B. L. Lin, C. R. Clough and G. L. Hillhouse, Interactions of Aziridines with Nickel Complexes: Oxidative-Addition and Reductive-Elimination Reactions That Break and Make C–N Bonds, *J. Am. Chem. Soc.*, 2002, **124**(12), 2890–2891, DOI: 10.1021/JA017652N.

46 S. Yu, T. Shin, M. Zhang, Y. Xia, H. Kim and S. Lee, Nickel/Briphos-Catalyzed Direct Transamidation of Unactivated Secondary Amides Using Trimethylsilyl Chloride, *Org. Lett.*, 2018, **20**(23), 7563–7566, DOI: 10.1021/ACS.ORGLETT.8B03304.

47 D. Yang, T. Shin, H. Kim and S. Lee, Nickel/Briphos-Catalyzed Transamidation of Unactivated Tertiary Amides, *Org. Biomol. Chem.*, 2020, **18**(31), 6053–6057, DOI: 10.1039/D0OB01271H.

48 L. Hie, N. F. Fine Nathel, T. K. Shah, E. L. Baker, X. Hong, Y. F. Yang, P. Liu, K. N. Houk and N. K. Garg, Conversion of Amides to Esters by the Nickel-Catalysed Activation of Amide C–N Bonds, *Nature*, 2015, **524**(7563), 79–83, DOI: 10.1038/NATURE14615.

49 B. J. Simmons, N. A. Weires, J. E. Dander and N. K. Garg, Nickel-Catalyzed Alkylation of Amide Derivatives, *ACS Catal.*, 2016, **6**(5), 3176–3179, DOI: 10.1021/ACSCATAL.6B00793.

50 N. A. Weires, E. L. Baker and N. K. Garg, Nickel-Catalysed Suzuki-Miyaura Coupling of Amides, *Nat. Chem.*, 2016, **8**(1), 75–79, DOI: 10.1038/NCHEM.2388.

51 J. E. Dander and N. K. Garg, Breaking Amides Using Nickel Catalysis, *ACS Catal.*, 2017, **7**(2), 1413–1423, DOI: 10.1021/ACSCATAL.6B03277.

52 J. E. Dander, E. L. Baker and N. K. Garg, Nickel-Catalyzed Transamidation of Aliphatic Amide Derivatives, *Chem. Sci.*, 2017, **8**(9), 6433–6438, DOI: 10.1039/C7SC01980G.

53 N. Moeini-Eghbali and H. Eshghi, Immobilized Nickel Nanoparticles on Modified Magnetic Titanium Dioxide: A Proficient and Eco-Friendly Nanocatalyst for the Green A3-Coupling Synthesis of Propargylamines, *J. Mol. Struct.*, 2024, **1305**, 137727, DOI: 10.1016/J.MOLSTRUC.2024.137727.

54 L. Truong-Phuoc, J. M. Nhut, L. Vidal, C. Duong-Viet, S. Sall, C. Petit, C. Sutter, M. Arab, A. Jourdan and C. Pham-Huu, Depleted Uranium Oxide Supported Nickel Catalyst for Autothermal CO_2 Methanation in Non-Adiabatic Reactor under Induction Heating, *J. Energy Chem.*, 2023, **85**, 310–323, DOI: 10.1016/J.JECHEM.2023.06.035.

55 I. M. S. Anekwe, M. Chetty, L. Khotseng, S. L. Kiambi, L. Maharaj, B. Oboirien and Y. M. Isa, Stability, Deactivation and Regeneration Study of a Newly Developed HZSM-5 and Ni-Doped HZSM-5 Zeolite Catalysts for Ethanol-to-Hydrocarbon Conversion, *Catal. Commun.*, 2024, **186**, 106802, DOI: 10.1016/J.CATCOM.2023.106802.

56 M. G. Gutierrez, Z. Theis, T. W. R. Lewis and D. J. Bellert, A Molecular Beam Apparatus for Performing Single Photon Initiated Dissociative Rearrangement Reactions (SPIDRR) with Transition Metal Cation Bound Organic Clusters, *Rev. Sci. Instrum.*, 2018, **89**(7), 074101, DOI: 10.1063/1.5024939.

57 J. E. Schneider, M. K. Goetz and J. S. Anderson, Variable Temperature Kinetic Isotope Effects Demonstrate Extensive Tunnelling in the C–H Activation Reactivity of a Transition Metal-Oxo Complex, *Chem. Commun.*, 2023, **59**(55), 8584–8587, DOI: 10.1039/D3CC02130K.

58 C. Whittington, J. Latham and A. R. Offenbacher, Tunneling through the Barriers: Resolving the Origins of the Activation of C–H Bonds Catalyzed by Enzymes, *ACS Symp. Ser.*, 2020, **1357**, 139–160, DOI: 10.1021/BK-2020-1357.CH007.

59 S. U. Okafor, G. Pinto, M. Brdecka, W. Smith, T. W. R. Lewis, M. Gutierrez and D. J. Bellert, Hydrogen Tunneling with an Atypically Small KIE Measured in the Mediated Decomposition of the $Co(CH_3COOH)^+$ Complex, *Phys. Chem. Chem. Phys.*, 2024, **26**(43), 27741–27750, DOI: 10.1039/D4CP02722A.

60 T. W. R. Lewis, E. M. Mastin, Z. C. Theis, S. U. Okafor, M. G. Gutierrez and D. J. Bellert, Two State Reactivity (TSR) and Hydrogen Tunneling Reaction Kinetics Measured in the Co + Mediated Decomposition of CH_3CHO, *Phys. Chem. Chem. Phys.*, 2023, **25**(35), 23477–23490, DOI: 10.1039/D2CP05042K.

61 M. E. Sanz, M. C. McCarthy and P. Thaddeus, Vibrational Excitation and Relaxation of Five Polyatomic Molecules in an Electrical Discharge, *J. Chem. Phys.*, 2005, **122**(19), 194319, DOI: 10.1063/1.1869988.

62 M. A. Ashraf, J. Kozubal and R. B. Metz, Bond Dissociation Energy and Electronic Spectroscopy of Cr + (NH_3) and Its Isotopomers, *J. Chem. Phys.*, 2018, **149**(17), 174301, DOI: 10.1063/1.5053691.

63 J. T. Stewart, B. E. Brumfield, B. M. Gibson and B. J. McCall, Vibrational Cooling of Large Molecules in Supersonic Expansions: The Case of C60 and Pyrene. Proceedings of the International Symposium of Molecular Spectroscopy, 2012, vol. 67, p. FB05.

64 R. L. Deleon and J. S. Muenter, Vibrational Relaxation of Linear Molecules in a Nozzle Expansion, *Chem. Phys. Lett.*, 1984, **111**(1–2), 147–150, DOI: 10.1016/0009-2614(84)80453-4.

65 C. S. Wang and J. Callaway, Band Structure of Nickel: Spin–Orbit Coupling, the Fermi Surface, and the Optical Conductivity, *Phys. Rev. B: Condens. Matter Mater. Phys.*, 1974, **9**(11), 4897, DOI: 10.1103/PhysRevB.9.4897.

66 A. Kramida, Yu. Ralchenko, J. Reader and NIST ASD Team, *NIST Atomic Spectra Database (ver. 5.12)*, 2024, [Online]. National Institute of Standards and Technology, Gaithersburg, MD, DOI: 10.18434/T4W30F.

67 R. L. Asher, D. Bellert, T. Buthelezi and P. J. Brucat, Spin forbidden transitions in $NiAr^+$, *Chem. Phys. Lett.*, 1994, **228**(6), 599–604, DOI: 10.1016/0009-2614(94)00995-3.

68 R. L. Asher, D. Bellert, T. Buthelezi, G. Weerasekera and P. J. Brucat, The binding energy of Ni + $\cdot CO_2$, *Chem. Phys. Lett.*, 1994, **228**(4–5), 390–392, DOI: 10.1016/0009-2614(94)00970-8.

69 J. S. Daluz, A. Kocak and R. B. Metz, Photodissociation Studies of the Electronic and Vibrational Spectroscopy of Ni + (H_2O), *J. Phys. Chem. A*, 2012, **116**(5), 1344–1352, DOI: 10.1021/JP211220V.

70 M. J. Frisch, *et al. Gaussian 16, Revision C.01*, Gaussian, Inc., Wallingford, CT, 2016.

71 R. E. Langer, On the Connection Formulas and the Solutions of the Wave Equation, *Phys. Rev.*, 1937, **51**(8), 669, DOI: 10.1103/PhysRev.51.669.

72 W. H. Miller, Quantum Mechanical Transition State Theory and a New Semiclassical Model for Reaction Rate Constants, *J. Chem. Phys.*, 1974, **61**(5), 1823–1834, DOI: 10.1063/1.1682181.

73 C. A. Gonzalez, T. C. Allison and F. Louis, General Expression for the Effective Mass in the One-Dimensional Treatment of Tunneling Corrections, *J. Phys. Chem. A*, 2001, **105**(49), 11034–11040, DOI: 10.1021/JP0115345.

74 R. T. Skodje, D. G. Truhlar and B. C. Garrett, A General Small-Curvature Approximation for Transition-State-Theory Transmission Coefficients, *J. Phys. Chem.*, 1981, **85**(21), 3019–3023, DOI: 10.1021/J150621A001.

75 D. G. Truhlar, Semiclassical Multidimensional Tunnelling Calculations, *RSC Theor. Comput. Chem. Ser.*, 2020, **2021**(18), 261–282, DOI: 10.1039/9781839160370-00261.

76 A. Fernandez-Ramos and D. G. Truhlar, Improved Algorithm for Corner-Cutting Tunneling Calculations, *J. Chem. Phys.*, 2001, **114**(4), 1491–1496, DOI: 10.1063/1.1329893.

77 A. Fernández-Ramos, D. G. Truhlar, J. C. Corchado and J. Espinosa-García, Interpolated Algorithm for Large-Curvature Tunneling Calculations of Transmission Coefficients for Variational Transition State Theory Calculations of Reaction Rates, *J. Phys. Chem. A*, 2002, **106**(19), 4957–4960, DOI: 10.1021/JP014204T.

78 M. M. Kreevoy, D. Ostović, D. G. Truhlar and B. C. Garrett, Phenomenological Manifestations of Large-Curvature Tunneling in Hydride-Transfer Reactions, *J. Phys. Chem.*, 1986, **90**(16), 3766–3774, DOI: 10.1021/J100407A052.

79 A. Fernández-Ramos and D. G. Truhlar, A New Algorithm for Efficient Direct Dynamics Calculations of Large-Curvature Tunneling and Its Application to Radical Reactions with 9-15 Atoms, *J. Chem. Theory Comput.*, 2005, **1**(6), 1063–1078, DOI: 10.1021/CT050153I.

80 R. Meana-Pañeda, D. G. Truhlar and A. Fernández-Ramos, Least-Action Tunneling Transmission Coefficient for Polyatomic Reactions, *J. Chem. Theory Comput.*, 2010, **6**(1), 6–17, DOI: 10.1021/CT900420E.

81 S. Battaglia, I. F. Galván and R. Lindh, Multiconfigurational Quantum Chemistry: The CASPT2 Method, *Theoretical and Computational Photochemistry: Fundamentals, Methods, Applications and Synergy with Experimental Approaches*, 2023, pp. 135–162, DOI: 10.1016/B978-0-323-91738-4.00016-6.

82 F. Neese, Software Update: The ORCA Program System—Version 5.0, *Wiley Interdiscip. Rev.: Comput. Mol. Sci.*, 2022, **12**(5), e1606, DOI: 10.1002/WCMS.1606.

83 F. Neese, F. Wennmohs, U. Becker and C. Riplinger, The ORCA Quantum Chemistry Program Package, *J. Chem. Phys.*, 2020, **152**(22), 224108, DOI: 10.1063/5.0004608/1061982.

84 F. Weigend, M. Häser, H. Patzelt and R. Ahlrichs, RI-MP2: Optimized Auxiliary Basis Sets and Demonstration of

Efficiency, *Chem. Phys. Lett.*, 1998, **294**(1–3), 143–152, DOI: 10.1016/S0009-2614(98)00862-8.

85 N. G. Hendricks and R. R. Julian, Leveraging Ultraviolet Photodissociation and Spectroscopy to Investigate Peptide and Protein Three-Dimensional Structure with Mass Spectrometry, *Analyst*, 2016, **141**(15), 4534–4540, DOI: 10.1039/C6AN01020B.

86 A. Agarwal, J. K. Diedrich and R. R. Julian, Direct Elucidation of Disulfide Bond Partners Using Ultraviolet Photodissociation Mass Spectrometry, *Anal. Chem.*, 2011, **83**(17), 6455–6458, DOI: 10.1021/AC201650V.

87 L. S. Kassel, Studies in Homogeneous Gas Reactions I, *J. Phys. Chem.*, 1928, **32**, 225–242, DOI: 10.1021/J150284A007.

88 O. K. Rice and H. C. Ramsperger, Theories of Unimolecular Gas Reactions at Low Pressures, *J. Am. Chem. Soc.*, 1927, **49**(7), 1617–1629, DOI: 10.1021/JA01406A001.

89 R. A. Marcus, Unimolecular Dissociations and Free Radical Recombination Reactions, *J. Chem. Phys.*, 1952, **20**(3), 359, DOI: 10.1063/1.1700424.

90 T. Beyer and D. F. Swinehart, Algorithm 448: Number of Multiply-Restricted Partitions, *Commun. ACM*, 1973, **16**(6), 379, DOI: 10.1145/362248.362275.

91 J. E. Lawrence and J. O. Richardson, Improved Microcanonical Instanton Theory, *Faraday Discuss.*, 2022, **238**(0), 204–235, DOI: 10.1039/D2FD00063F.

92 W. H. Miller, Tunneling Corrections to Unimolecular Rate Constants, with Application to Formaldehyde, *J. Am. Chem. Soc.*, 1979, **101**(23), 6810–6814, DOI: 10.1021/JA00517A004.

93 W. H. Thompson, Quantum Mechanical Transition State Theory and Tunneling Corrections, *J. Chem. Phys.*, 1999, **110**(9), 4221–4228, DOI: 10.1063/1.478304.

94 A. Fernandez-Ramos, B. A. Ellingson, B. C. Garrett and D. G. Truhlar, Variational Transition State Theory with Multidimensional Tunneling, *Rev. Comput. Chem.*, 2007, **23**, 125–232, DOI: 10.1002/9780470116449.CH3.

95 D. S. King, M. R. Hermes, D. G. Truhlar and L. Gagliardi, Large-Scale Benchmarking of Multireference Vertical-Excitation Calculations via Automated Active-Space Selection, *J. Chem. Theory Comput.*, 2022, **18**(10), 6065–6076, DOI: 10.1021/ACS.JCTC.2C00630.

96 M. Feldt and Q. M. Phung, Ab Initio Methods in First-Row Transition Metal Chemistry, *Eur. J. Inorg. Chem.*, 2022, (15), e202200014, DOI: 10.1002/EJIC.202200014.

97 X. Gao, X. Y. Yu and C. R. Chang, Perceptions on the Treatment of Apparent Isotope Effects during the Analyses of Reaction Rate and Mechanism, *Phys. Chem. Chem. Phys.*, 2022, **24**(25), 15182–15194, DOI: 10.1039/D2CP00825D.

98 T. Hama, H. Ueta, A. Kouchi and N. Watanabe, Quantum Tunneling Observed without Its Characteristic Large Kinetic Isotope Effects, *Proc. Natl. Acad. Sci. U. S. A.*, 2015, **112**(24), 7438–7443, DOI: 10.1073/PNAS.1501328112.

99 M. Ertelt, D. A. Hrovat, W. T. Borden and W. Sander, Heavy-Atom Tunneling in the Ring Opening of a Strained Cyclopropene at Very Low Temperatures, *Chem. – Eur. J.*, 2014, **20**(16), 4713–4720, DOI: 10.1002/CHEM.201303792.

100 O. M. Gonzalez-James, X. Zhang, A. Datta, D. A. Hrovat, W. T. Borden and D. A. Singleton, Experimental Evidence for Heavy-Atom Tunneling in the Ring-Opening of Cyclopropylcarbinyl Radical from Intramolecular $^{12}C/^{13}C$ Kinetic Isotope Effects, *J. Am. Chem. Soc.*, 2010, **132**(36), 12548–12549, DOI: 10.1021/JA1055593.

101 X. D. Zhu, A. Lee, A. Wong and U. Linke, Surface Diffusion of Hydrogen on Ni(100): An Experimental Observation of Quantum Tunneling Diffusion, *Phys. Rev. Lett.*, 1992, **68**(12), 1862, DOI: 10.1103/PhysRevLett.68.1862.

102 A. Lee, X. D. Zhu, L. Deng and U. Linke, Observation of a Transition from Over-Barrier Hopping to Activated Tunneling Diffusion: H and D on Ni(100), *Phys. Rev. B: Condens. Matter Mater. Phys.*, 1992, **46**(23), 15472, DOI: 10.1103/PhysRevB.46.15472.

103 S. E. Wonchoba, W. P. Hu and D. G. Truhlar, Surface Diffusion of H on Ni(100): Interpretation of the Transition Temperature, *Phys. Rev. B: Condens. Matter Mater. Phys.*, 1995, **51**(15), 9985, DOI: 10.1103/PhysRevB.51.9985.